ACS APPLIED MATERIALS & INTERFACES

Research Article

www.acsami.org

In-Situ Generation of Oxide Nanowire Arrays from AgCuZn Alloy Sulfide with Enhanced Electrochemical Oxygen-Evolving Performance

Minghao Xie, Shiqi Ai, Jian Yang, Yudi Yang, Yihan Chen, and Yong Jin*

Department of Materials Science and Engineering, Sichuan University, Chengdu 610064, People's Republic of China

Supporting Information

ABSTRACT: In this study, AgCuZn sulfide is fabricated on the surface of AgCuZn alloys by hydrothermal sulfuration. This ternary metal sulfide is equipped with enhanced activity toward oxygen evolution reaction (OER) in an alkaline electrolyte. Through comparison of the alloys with diverse compositions, we find out the best electrochemical property of a particular alloy sulfide forming on a AgCuZn substrate (Ag:Cu:Zn = 43:49:8). The alloy sulfide exhibits an onset overpotential (η) of 0.27 V with a Tafel slope of 95 ± 2 mV dec^{-1} and a current density of 130 mA cm^{-2} at η of 0.57 V. Moreover, the obtained AgCuZn sulfide displays excellent stability, where the current density can increase to 130% of the initial value after a water electrolysis test for 100 000 s (27.7 h). Through investigating the electrode before and after the electrocatalysis, we find a remarkable activated process during which self-supported copper−silver oxide nanowire (CuO−Ag_2O NW) arrays in situ form on the surface of the electrode. This work provides a feasible strategy for synthesis of high performance nonprecious metal electrocatalysts for water splitting.

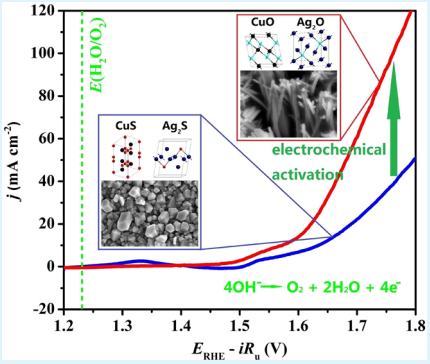

KEYWORDS: *in-situ generation, oxygen evolution reaction, alloy sulfides, nanowire arrays, electrochemistry*

1. INTRODUCTION

The large-scale electrolysis of water for hydrogen evolution reaction (HER) needs better catalysts to reduce the dynamic load related to oxygen evolution reaction (OER). Therefore, efficient OER catalysts designed with low-cost and abundant sources are very important sources of sustainable energy. Although current developments in the study of heterogeneous catalytic materials promote the OER (eqs 1 and 2; E° is the standard potential and NHE is the normal hydrogen electrode),[1−5] a mass of commercial electrolytic cells have been hampered for lack of low-cost catalysts which display high current densities at low overpotentials (η) over durable periods of time.

$$2H_2O(l) \rightarrow O_2(g) + 4H^+(aq) + 4e^- \quad (1)$$

$$E^\circ(O_2/H_2O) = 1.23\ \text{V versus NHE} \quad (2)$$

The above equations show that OER is a process which includes the transfer of four protons and four electrons, and slow oxygen evolution kinetics usually require a high electrochemical η for the purpose of impelling the reaction at practical rates.[6] As a half reaction of splitting water into oxygen and protons, OER plays a significant role in diverse significant energy conversion and storage systems.[7−14]

However, so far there is still no ideal OER catalyst which perfectly fulfills all of the requirements already mentioned. A variety of perovskite,[15] spinel[16] solids, and some compounds containing transition metals (e.g., Co, Ni, and W) have been widely applied in electrocatalysis.[17−22] Current research has found out that metal oxides as water oxidation catalysts exhibit excellent activity and durability.[3,12,23] Among metal oxides, IrO_2 and RuO_2 have proved to be the best OER catalysts.[24,25] However, considering the cost of the catalysts which help to split water to oxygen, we should find some less expensive and more earth-abundant materials in the domain of metals. On the basis of these reasons, some compounds and materials containing these metals ought to be further studied as OER catalysts in alkaline aqueous solutions. In recent years, polymetallic oxides have been discovered as favorable electrodes for catalytic materials.[26−31] Our recent study reported a kind of mixed copper−silver oxide nanowires (CuO−Ag_2O NWs) which are in situ generated on the surface of AgCuZn alloys through direct oxidation by Na_2O_2.[32] The growth process of the nanowires on the AgCuZn substrates encompasses cocrystallization of copper oxide and silver oxide into heterostructured oxides with decrease of activation energy by sacrifice of zinc. Moreover, the obtained CuO−Ag_2O NWs display an improved electrocatalytic activity for water oxidation at room temperature.

Metal sulfides have been recognized as a new type of semiconductor material, of which the catalytic property is the focus of current research.[33−39] However, studies about

Received: May 1, 2015
Accepted: July 16, 2015
Published: July 16, 2015

DOI: 10.1021/acsami.5b03805
ACS Appl. Mater. Interfaces 2015, 7, 17112−17121

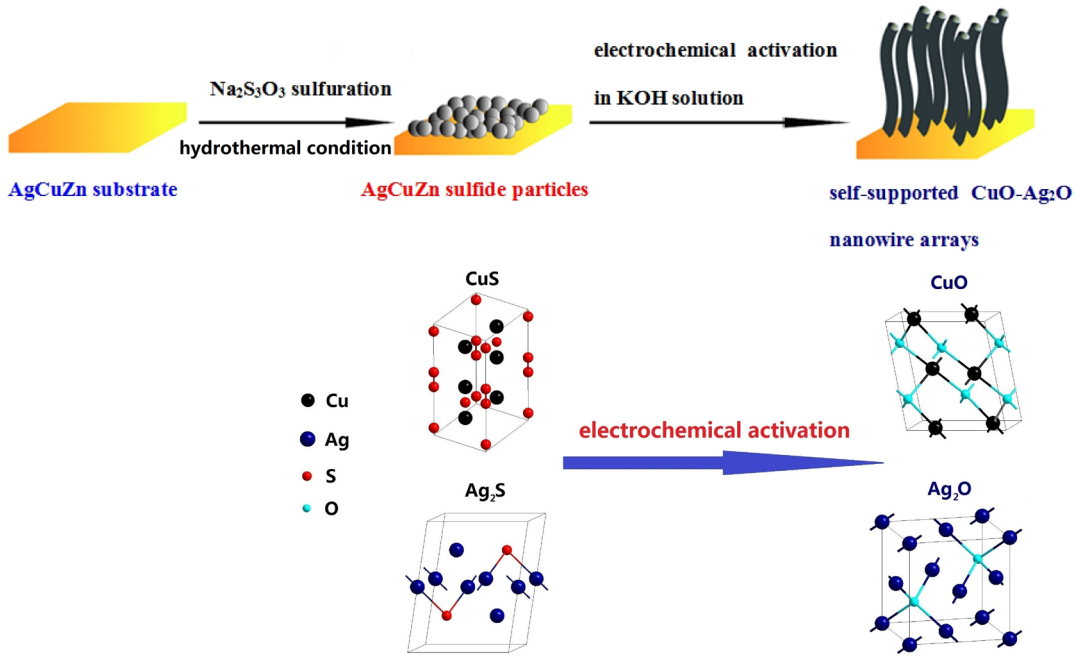

Figure 1. Schematic process of the whole course for the changes on the surface of the AgCuZn substrate and the changes of crystal structures during the activated process.

polymetallic sulfides have rarely been reported. Herein, we synthesize ternary metal sulfide on the AgCuZn alloys via a facile hydrothermal sulfuration method. The AgCuZn sulfide electrode shows excellent electrocatalytic activity and stability toward water oxidation under an alkaline condition. Furthermore, we optimize the catalytic property of the alloy sulfide electrode by changing the AgCuZn substrates with diverse metallic proportions. The catalytic process of the AgCuZn sulfide is investigated by systematically studying this electrode catalyst before and after electrolysis of water. The results show that there exists an obvious electrochemical activation on the electrode during the catalytic process. The as-prepared ternary metal sulfide electrode exhibits superior electrochemical performance as a catalytic material for water oxidation, which indicates the extensive applicability of this method for obtaining novel alloy oxide nanowires as OER catalysts.

2. EXPERIMENTAL SECTION

2.1. Synthesis of AgCuZn Sulfide Electrode. All reagents were analytically pure grade and were used without further purification. In a typical preparation, AgCuZn alloy rods with various metallic proportions were gained through an intermediate frequency furnace, with the field frequency at 400 Hz.[40] Before the hydrothermal process, the alloy rods were rubbed with abrasive paper and were cleaned in absolute ethyl alcohol in an ultrasonic bath for 2 min. Then, an alloy rod with a specific proportion, 15 mL 0.20 M freshly prepared $Na_2S_2O_3 \cdot 5H_2O$ (Dagu Chemical Corporation, China) aqueous solution, and 1 mL strong aqua ammonia were put into a Teflon-lined stainless steel autoclave of 25 mL volume, which was filled with solution up to 80% of the total capacity. The autoclave was sealed and heated at 180 °C for 12 h, and then it was allowed to cool at room temperature naturally. Finally, the as-prepared electrode was washed sequentially with deionized water and absolute ethanol and was dried in the air at room temperature.

2.2. Synthesis of Single Metal Sulfide Electrodes and RuO_2 Electrode. Single metal sulfides including silver sulfide and copper sulfide were fabricated using a silver sheet and a copper sheet as the respective substrate through the same process described earlier. Ten microliters of ink of a solution composed of 5 mg commercial RuO_2 (Alfa Aesar, U.K.), 140 μL isopropanol, 360 μL deionized water, and 5 μL Nafion was dropped on a carbon fiber paper with a mass loading of 0.4 mg cm^{-2} and was dried in the air for hours as RuO_2 working electrode.

2.3. Material Characterization. The morphology of the catalyst forming on the surface of the alloy electrode was investigated using a scanning electron microscope (SEM; Hitachi S4800, Japan) with an accelerating voltage of 5.0 kV. The high-resolution transmission electron microscopy (HRTEM) images were collected with an FEI Tecnai G2 F20 S instrument at 200 kV. The elements and compositions of the surface substances on the ternary alloy electrode before and after the electrocatalysis were analyzed using X-ray diffraction (XRD; Fangyuan DX-1000, China) and energy-dispersive X-ray spectrometry (EDS). XRD analyses of the electrode catalyst were collected with Cu Kα radiation at 40 kV. The sample for XRD was alloy sheet produced by the same process. EDS was performed by an EDAX detector (EDAX Corp., USA). X-ray photoelectron spectroscopy (XPS) patterns were acquired on a Thermo VG Scientific ESCALab 250 XPS spectrometer (Waltham, MA, USA) equipped with a Mg K X-ray (1253.6 eV) excitation source running at 15 kV.

2.4. Electrochemical Measurements. Electrochemical properties of the as-obtained electrode were measured by a electrochemical workstation (LK9805, Tianjin Lanlike Corp., China) at room temperature. Electrochemical measurements were made in a standard three-electrode system, where the obtained AgCuZn alloy sulfide was used as the working electrode. The effective tested area of working electrode was controlled with the diameter of 2 mm and the immersing length of 5 mm. Pt and a Hg/HgO electrode served as the counter electrode and the reference electrode, respectively. The 1.0 M KOH (Kelong Chemical Factory, China) solution was used as

DOI: 10.1021/acsami.5b03805
ACS Appl. Mater. Interfaces 2015, 7, 17112−17121

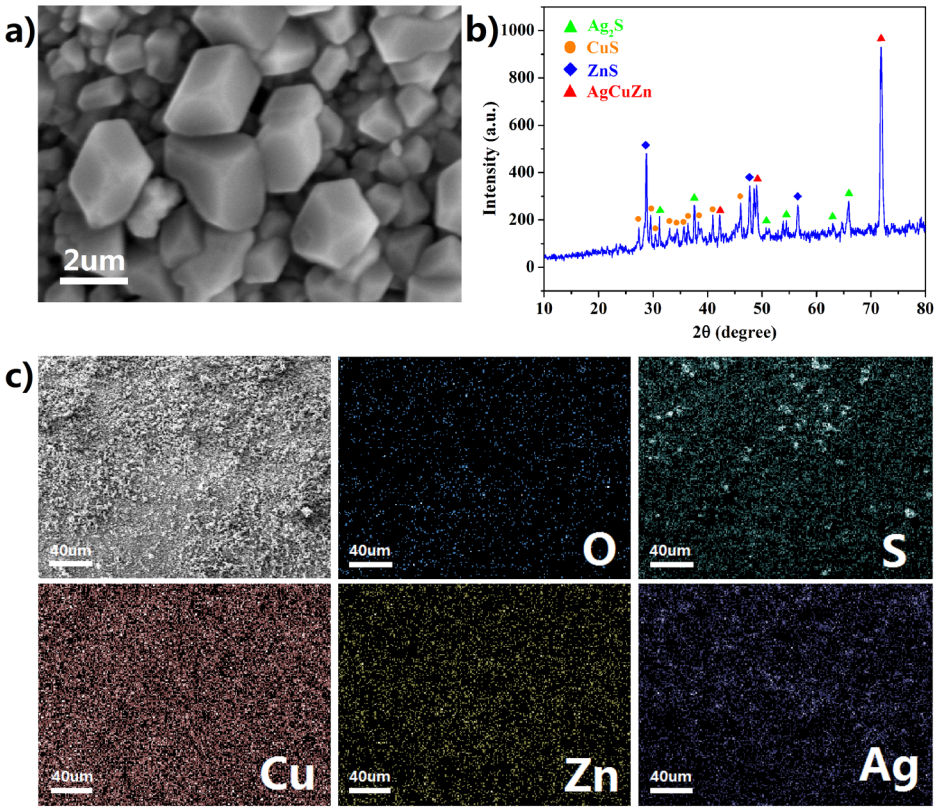

Figure 2. (a) SEM image of the AgCuZn sulfide particles forming on the alloy substrate. (b) XRD pattern of CuS, ZnS, and Ag_2S after hydrothermal process. (c) Elemental mapping of the elements on the surface of the AgCuZn alloy after hydrothermal sulfuration.

the electrolyte. All electrochemical potentials were revised with uncompensated solution resistance (R_u, here R_u was fixed to 2 Ω which is measured by the high-frequency pulse function) and are provided in the text and figures versus the reversible hydrogen electrode [eq 3; E_{RHE} is the potential vs reversible hydrogen electrode; E is the directly measured potential (V vs Hg/HgO); and $E_{Hg/HgO}$ is the standard electrode potential of Hg/HgO electrode vs normal hydrogen electrode, which is used as 0.092 V]:

$$E_{RHE} = E + E_{Hg/HgO} + 0.059\ pH \quad (3)$$

The electrochemical impedance spectroscopy (EIS) was recorded using the electrochemical workstation (Autolab PGSTAT 12 potentiostat/galvanostat, Netherlands). Faradaic efficiency test was conducted by oxygen gas sensor (PASCO, USA) which measured the dissolved oxygen gas concentration in the solution, and the integral molar quantity of evolved oxygen versus time was computed according to Henry's law. All of the alloy sulfide electrodes were tested after activation by cyclic voltammetry (CV) for 20 cycles over a potential range of 1.0−2.0 V (versus RHE) under a scan rate of 50 mV s^{-1} (~800 s) until the current density stopped increasing greatly. All of the electrochemical measurements were performed at room temperature.

3. RESULTS AND DISCUSSION

3.1. Characterization of the Electrode Catalyst. The whole course of the chances on the surface of the AgCuZn substrate is displayed in Figure 1. First, alkaline hydrothermal condition impels CuS, Ag_2S, and ZnS to crystallize as particles. Then, self-supported CuO−Ag_2O NW arrays grow during electrochemical activation in KOH solution. Furthermore, the changes of the crystal structures during the activated process is also shown in Figure 1.

The morphology and structure on the surface of the AgCuZn electrode are studied by scanning electron microscopy (SEM) and high-resolution transmission electron microscopy (HRTEM). Figure 2a shows the SEM image of the AgCuZn electrode after the hydrothermal process. Through the hydrothermal process, CuS, Ag_2S, and ZnS with the structure of particles crystallize on the AgCuZn alloy, of which the diameters range from 500 nm to 5 um. The HRTEM images of the AgCuZn sulfide particles are shown in Figure S1 in the Supporting Information (SI).

Figure 2b shows the X-ray diffraction (XRD) pattern of the substances on the surface of the electrode after the hydrothermal process. It reveals that there are only CuS, Ag_2S, and ZnS on the AgCuZn alloy electrode. The XRD patterns of the respective Ag sulfide and Cu sulfide are given in Figure S2 of the SI. The elemental composition and distribution on the alloy electrode are shown in the elemental mapping (Figure 2c). The results suggest that $Na_2S_2O_3$ is gradually discomposed under a hydrothermal condition with strong aqua ammonia providing an alkaline condition, which generates abundant sulfur. The hydrothermal condition forces sulfur atoms to enter into the lattice of AgCuZn alloy, which impels the formation of the crystal nucleus of CuS, Ag_2S, and ZnS and the growth of their crystals with simple processes listed below:

$$Na_2S_2O_3 \rightarrow Na_2SO_3 + S \quad (4)$$

$$Zn + S \rightarrow ZnS \quad (5)$$

$$2Ag + S \rightarrow Ag_2S \quad (6)$$

DOI: 10.1021/acsami.5b03805
ACS Appl. Mater. Interfaces 2015, 7, 17112−17121

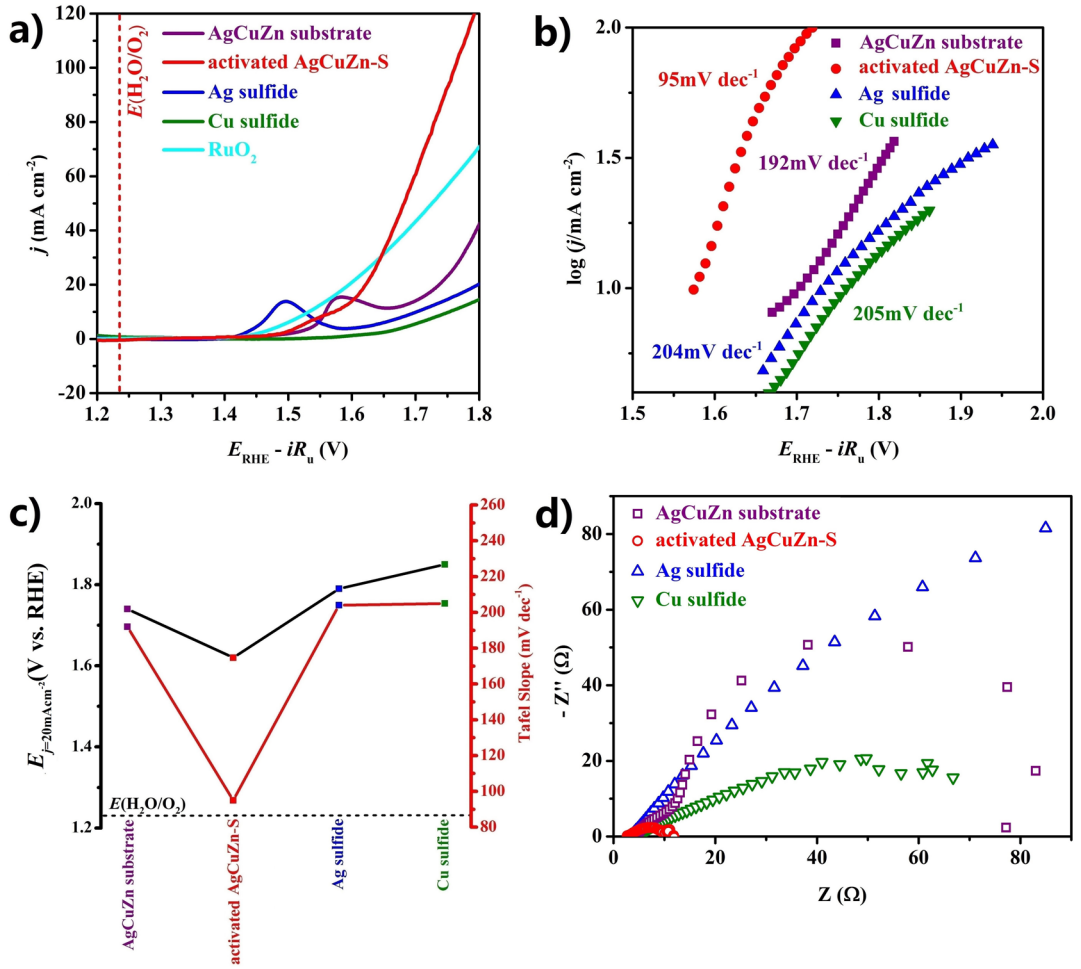

Figure 3. (a) LSV curves of AgCuZn sulfide after electrochemical activation by CV curves (activated AgCuZn−S), bare AgCuZn alloy substrate, Ag sulfide, Cu sulfide, and RuO_2. (b) Tafel plots displaying the superior catalytic activity of activated AgCuZn sulfide to single metal sulfides. (c) Tafel slopes and E_{RHE} required to reach j = 20 mA cm^{-2} ($E_{j=20mAcm^{-2}}$) for the four kinds of electrodes. (d) EIS spectra of the four kind of electrodes. The dash lines indicate the theoretical value of thermodynamic potential for water oxidation.

$$Cu + S \rightarrow CuS \quad (7)$$

Under hydrothermal condition with $Na_2S_2O_3$ serving as sulfur source (eq 4), Zn, Ag, and Cu atoms take part in the sulfuration reactions (eqs 5−7). Then, ZnS, CuS and Ag_2S are shaped with the structure of particles under sulfur-rich hydrothermal condition.

3.2. Electrochemical Performances. The catalytic properties of the ternary metal sulfide for water oxidation are measured by examinations of linear sweep voltammetry (LSV) and cyclic voltammetry (CV). All of the electric polarization curves of the alloy sulfide electrodes are collected after electrochemical activation by CV until the current density becomes steady. The detailed process of the electrochemical activation is provided in Figure S3 of the SI.

All of the oxidation current is normalized to the geometric area, which means that the current density (j) can be directly used for the comparison of the catalytic activity for different electrode samples. Faradaic efficiency test of activated AgCuZn sulfide is carried out in 300 s, and the result reveals that the ratio of released oxygen between the experimental value and the theoretical value is nearly 100% (Figure S4 of the SI). The electrochemical behaviors of bare AgCuZn alloy substrate, activated AgCuZn sulfide, Ag sulfide, and Cu sulfide are shown in Figure 3a. The bare alloy substrate shows an onset potential of 1.66 ± 0.02 V (versus RHE) with a Tafel slope of 192 ± 6 mV decade^{-1}. The unsatisfied water oxidation activity of the bare alloy substrate indicates the limited contribution of the substrate for the catalytic activity of the activated alloy sulfide. To compare the alloy sulfide electrode with single metal sulfides, Ag sulfide and Cu sulfide are prepared through the same process with AgCuZn sulfide and exhibit a very poor OER activity. Remarkably, activated AgCuZn sulfide displays the lowest onset potential (~1.50 V) in the four kinds of electrodes. The LSV of activated AgCuZn sulfide reveals a small rise in current density at 1.51 ± 0.01 V (η = 0.28 V), following a small peak which corresponds to the oxidation of Cu(II) and Ag(I) to Cu(III) and Ag(II), respectively.[41,42] Then, a rapid increase in current density occurs at 1.62 ± 0.01 V (η = 0.39 V), corresponding to catalytic water oxidation. Also, the activated alloy sulfide catalyst exhibits the highest electrocatalytic activity with a current density of ~130 mA cm^{-2} at ~1.8 V (η = 0.57 V). Also, compared with the commercial RuO_2 which displays a lower onset potential (~1.46 V), the activated AgCuZn sulfide exhibits a much faster increase of current density at high η (>0.42 V). Plus, the comparison of CV curves for the four kinds of electrodes (bare AgCuZn alloy substrate, activated AgCuZn sulfide, Ag sulfide, and Cu sulfide) recorded in 1.0 M KOH solution is presented in Figure S5 of

DOI: 10.1021/acsami.5b03805
ACS Appl. Mater. Interfaces 2015, 7, 17112−17121

the SI. As shown in Figure 3b, activated AgCuZn sulfide gained a lower Tafel slope (~95 mV decade^{-1}) at low η (~0.39 V) than that measured with Ag sulfide (~204 mV decade^{-1}) and Cu sulfide (~205 mV decade^{-1}), further demonstrating the superior electrocatalytic activity of the ternary metal sulfide relative to single metal sulfides. Figure 3c displays direct comparisons of the Tafel slopes and potentials (E_{RHE}) required to reach j = 20 mA cm^{-2} for the four kinds of electrodes. As another comparison, electrochemical impedance spectroscopy (EIS) for the four kinds of electrodes is collected in 1.0 M KOH electrolyte (Figure 3d). It shows that the activated AgCuZn sulfide as an OER catalyst possesses a much smaller semicircle than other electrode catalysts, indicating a lower charge-transfer resistance (R_{ct}) of activated AgCuZn sulfide in the system, since the alloy sulfide is an excellent electric conductor which enables it to pass electrons more effectively.

For more comparison, Table S1 in the SI lists the quantitative values of η when the current density reaches 5 mA cm^{-2}, 10 mA cm^{-2}, and Tafel slope of all the prepared OER electrodes along with 20 wt % Ir/C and 20 wt % Ru/C on glass carbon electrodes (with the metal concentration of ~28 μg cm^{-2}) according to reported articles.[43] As the benchmark catalysts for OER, 20 wt % Ir/C and 20 wt % Ru/C possess excellent activity for OER. However, the values of η when the current density reaches 5 mA cm^{-2}, 10 mA cm^{-2}, and Tafel slope of activated AgCuZn sulfide are all lower than these two catalytic materials, revealing the superiority of the activated AgCuZn sulfide as an OER catalyst.

Figure 4a and b gives a general range of the compositions of the AgCuZn alloy. Several trends in the kinetic parameters of the ternary metal compounds with different compositions are shown in the triangular coordinate plots. To obtain an accurate value of the best alloy composition, we prepare a lot of alloy substrates with various proportions and similarly calculate the elemental percentage of each by energy-dispersive X-ray spectrometry (EDS). In Figure 4a, the alloy compositions in the red zone correspond to the lowest Tafel slopes, and the proportion of the tested AgCuZn sulfide electrode focuses on this zone. Finally, we choose the alloy sulfide on the AgCuZn substrate with a mass ratio of 43%:49%:8% as mainly the investigated electrode.

Figure 4b shows the relationship between E_{RHE} required to reach j = 50 mA cm^{-2} and a general range of the compositions of the alloy. We also list the relationships between the onset potentials (E_{cat}), E_{RHE} when j is 40 mA cm^{-2} and 50 mA cm^{-2}, j when E_{RHE} is 1.8 V, and the amount of the three metals in the alloy sulfides. The detailed data of these relationships are shown in Table S2 of the SI. Plus, the LSV curves of the alloy electrodes with different metallic proportions, Cu sulfide, and Ag sulfide are shown in Figure S6 of the SI.

3.3. Investigation of the Activated Process. Because of the excellent activity of the activated AgCuZn sulfide electrode toward water oxidation under an alkaline condition, it is crucial to confirm the mechanism of the activated process. First, we compare polarization curves of the electrode before and after activation and find that the current density increases greatly after activation. Then, we analyze the microstructure and composition of it before and after activation through several characterization methods.

XRD patterns of the alloy electrode before and after activation demonstrate that two kinds of oxides including CuO and Ag_2O in situ form on the electrode along with the oxidation of water (Figure 5a). X-ray photoelectron spectroscopy (XPS) is used to measure the changes of the binding energies of the bonds in the sulfide and oxide on the alloy electrode before and after activation. Figure 5b displays the XPS results of the electrode before and after the activation process. The results reveal a positive shift of the binding energy of Cu 2p and Ag 3d along with the absence of the sulfur element and the presence of the oxygen element after activation, demonstrating a transformation from sulfide to oxide on the electrode after oxidation in 1.0 M KOH solution. The peaks of the Cu(II)−O bond are discovered at 934.5 and 954.4 eV, corresponding to Cu $2p_{3/2}$ and Cu $2p_{1/2}$ (Figure 5c).[44] The peak-fit of Cu $2p_{3/2}$ reveals a major peak at 934.5 eV along with several satellites on the sides of high-binding energy, 940.9 and 943.5 eV.[45] The peaks of the Ag−O are found at 368.1 and 374.2 eV, corresponding to Ag 3d,[46,47] after activation in KOH solution, while CuS and Ag_2S is detected before the activation (Figure 5c and d).[48,49] For more information, the EDS spectrum and the exact proportion of each element on the AgCuZn sulfide electrode before the activation process are displayed in Figure S7 and Table S3 of the SI.

SEM images and elemental mapping of the electrode after the activation process are displayed in Figure 6, from which we can observe obvious transformations of microstructure and element on the surface of the AgCuZn alloy. Myriad nanowire arrays arise instead of the original mixed sulfide particles, of which the diameters are ~100 nm with the lengths ranging

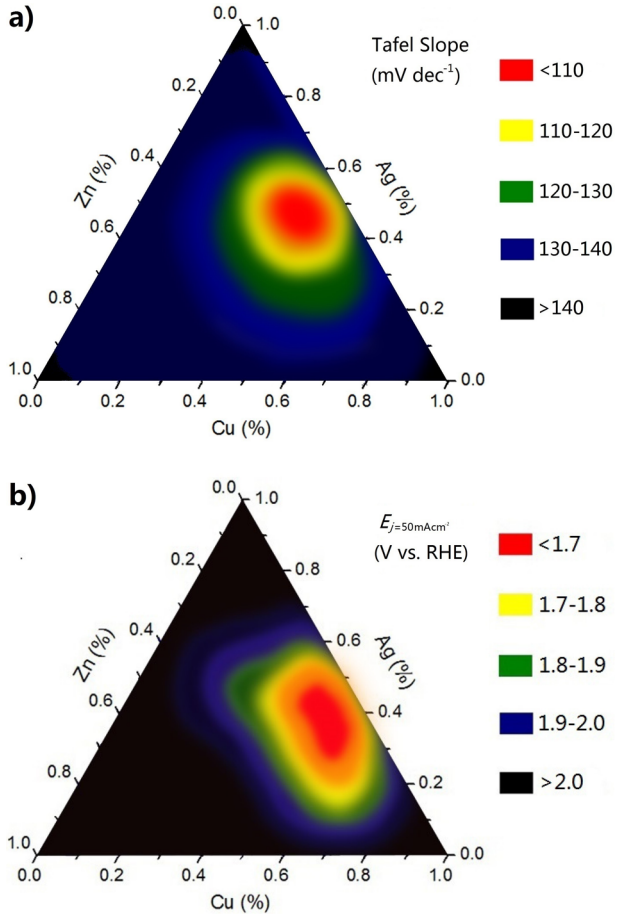

Figure 4. Triangular coordinate plots showing the relationships between the proportions of AgCuZn and (a) the Tafel slopes and (b) E_{RHE} required to reach j = 50 mA cm^{-2} ($E_{j=50mAcm^{-2}}$).

DOI: 10.1021/acsami.5b03805
ACS Appl. Mater. Interfaces 2015, 7, 17112−17121

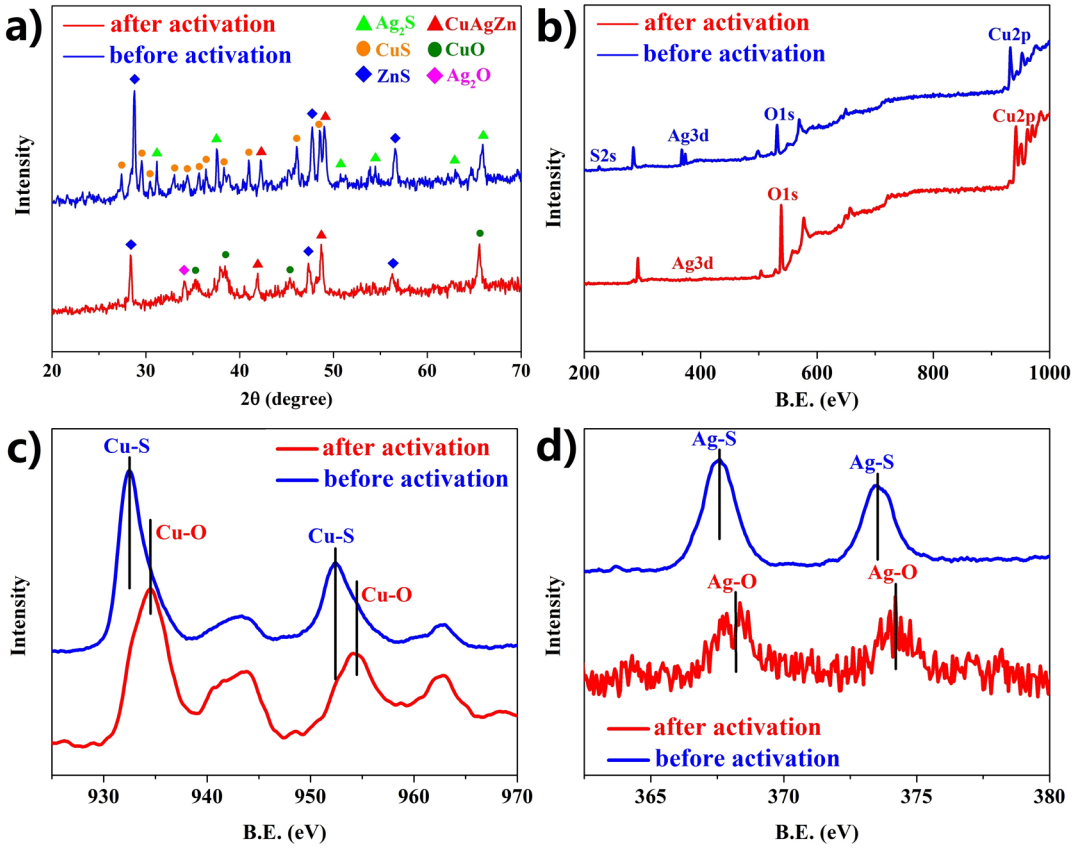

Figure 5. (a) XRD patterns of the substances on the electrode surface before and after the activation process in KOH solution. (b) XPS spectra showing the change of binding energies of the surface substances on the electrode before (blue solid line) and after (red solid line) the activation process. (c) XPS spectra showing the change of binding energies of Cu $2p_{3/2}$ and Cu $2p_{1/2}$ in the surface substances before (blue solid line) and after (red solid line) the activation process. (d) XPS spectra showing the change of binding energies of Ag 3d in the surface substances before (blue solid line) and after (red solid line) the activation process.

from 10 um to 20 um. The HRTEM images of the nanowire arrays are shown in Figure S8 of the SI. The images show that there exists a heterostructure which contains different phases (CuO and Ag_2O) recognized according to lattice distances in an individual nanowire. The results suggest that in the oxygen-rich alkaline aqueous solution which is provided by the oxidation of OH^-, sulfur atoms in the lattice are replaced by oxygen atoms to impel CuO and Ag_2O to crystallize with a structure of nanowire arrays. Reactions occurring in parallel under this condition are listed below:

$$4OH^- \rightarrow O_2 + 2H_2O + 4e^- \quad (8)$$

$$ZnS + 4OH^- \rightarrow ZnO_2^{2-} + 2H_2O + S + 2e^- \quad (9)$$

$$Ag_2S + 2OH^- \rightarrow Ag_2O + S^{2-} + H_2O \quad (10)$$

$$CuS + 2OH^- \rightarrow CuO + S^{2-} + H_2O \quad (11)$$

Abundant oxygen is generated during the oxidation of KOH solution (eq 8). Then, ZnS molecules are corroded by OH^- (eq 9), since zinc is an amphoteric metal which is dissolved as ZnO_2^{2-} under strong alkaline conditions.[32,40] The sacrificial zinc produces a large number of cavities and lattice imperfections. In a succedent process, CuS and Ag_2S molecules take part in the oxidation reaction (eqs 10 and 11) with CuO–Ag_2O nanowire (NW) arrays growing on the electrode.

Figure 7a shows the LSV curves of the AgCuZn sulfide (AgCuZn–S) before and after activation. Because the surface of the electrode is not absolute sulfide, the two small peaks of the LSV curve of AgCuZn–S before activation corresponds to complete oxidation of alloy substrate between 1.2 and 1.6 V versus RHE. The inset of Figure 7a reveals the change of current of AgCuZn–S during the drastic activation process of 800 s in an electrolysis of water test. The increase of the current density after activation as displayed by the prepared electrode is due to the gradual self-growing of CuO–Ag_2O NW arrays. In the CuO–Ag_2O NW arrays system, metal cations with high valences [Cu(III)/(IV), Ag(II)/(III)] are generated under a high anodic potential, which possess a synergistic effect as the active centers toward water oxidation.[32,42,50] The comparison of CV curves of AgCuZn–S before and after activation is also provided in Figure S9 of the SI. Further, we study the electric conductivity of AgCuZn–S before and after activation in KOH solution through EIS (Figure 7b). It reveals that the R_{ct} of AgCuZn–S has greatly decreased after the activation process, proving that the rate of charge transfer for activated AgCuZn–S becomes much faster and efficient.

3.4. Comparison of CuO–Ag_2O NWs Na_2O_2 and in-Situ Formation. Our works are based on the improvement of the OER activity of CuO–Ag_2O NWs prepared in oxygen-rich Na_2O_2 alkaline solution.[32] The electrochemical performances of CuO–Ag_2O NWs in situ forming via oxidation by Na_2O_2 (CuO–Ag_2O NWs–Na_2O_2) and self-supported CuO–Ag_2O NW arrays growing during activation of AgCuZn sulfide particles (activated AgCuZn–S) are separately tested in the same alkaline medium. The catalytic activity is evaluated by the

DOI: 10.1021/acsami.5b03805
ACS Appl. Mater. Interfaces 2015, 7, 17112–17121

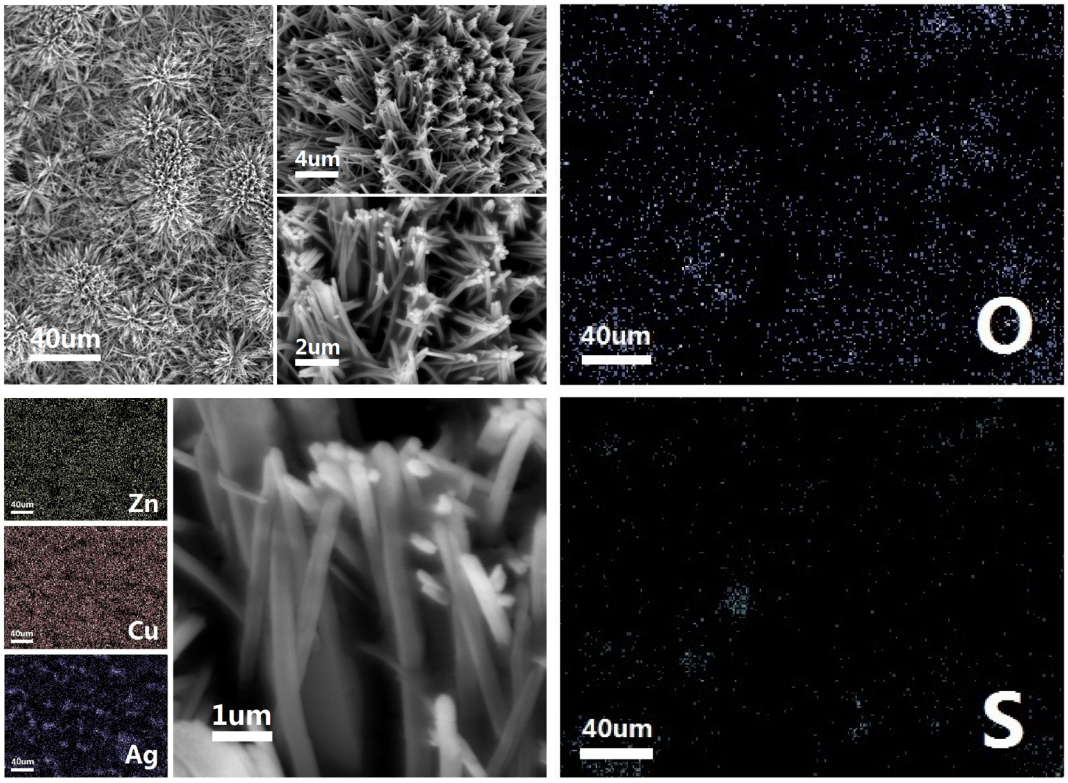

Figure 6. SEM images of the self-supported CuO−Ag_2O nanowire arrays and elemental mapping of the elements on the surface of the AgCuZn alloy after the activation process.

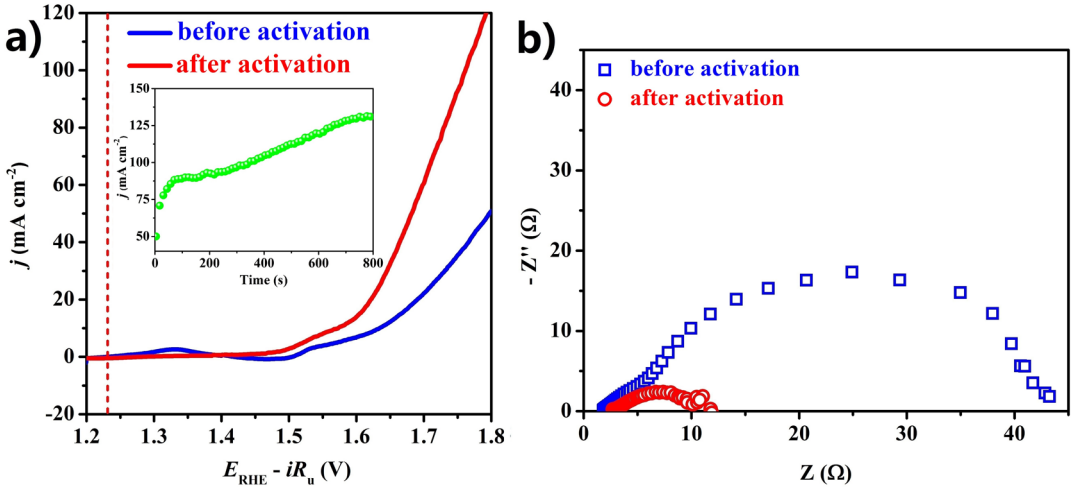

Figure 7. (a) LSV curves of AgCuZn−S before and after activation. The inset is the change of the current density of AgCuZn−S during the activation process of 800 s. The electrolysis test is maintained at 1.8 V versus RHE in 1.0 M KOH electrolyte. (b) EIS spectra of AgCuZn−S before and after activation.

LSV and Tafel plot, as shown in Figure 8a and b. The CV curves of the CuO−Ag_2O NWs−Na_2O_2 and activated AgCuZn−S are presented in Figure S10 of the SI. Also, we compare the electroactive areas of four electrode samples recorded in 1.0 M KOH solution (Figure 8c). The four samples are bare AgCuZn alloy substrate, CuO−Ag_2O NWs−Na_2O_2, AgCuZn−S, and activated AgCuZn−S. The electric double layer capacitance (C_d) is proportional to the electroactive area.[51] Figure 8c shows the obviously larger C_d ofactivated AgCuZn−S relative to that of the other samples, which reveals the great enhancement of active points on AgCuZn sulfide particles after the activation process.

To assess the electrocatalytic activity and long-term stability of activated AgCuZn−S (after activation for 800 s in Figure 7a) under a consecutive operational condition, electrolysis of water tests are conducted in 1.0 M KOH electrolyte. Figure 8d shows the current densities of CuO−Ag_2O NWs−Na_2O_2 and activated AgCuZn−S, which is recorded at 1.8 V versus RHE for 100 000 s (27.7 h). It is found that the current density of activated AgCuZn−S keeps increasing greatly in the initial 500 s (inset of Figure 8d), following a small and steady increase

DOI: 10.1021/acsami.5b03805
ACS Appl. Mater. Interfaces 2015, 7, 17112−17121

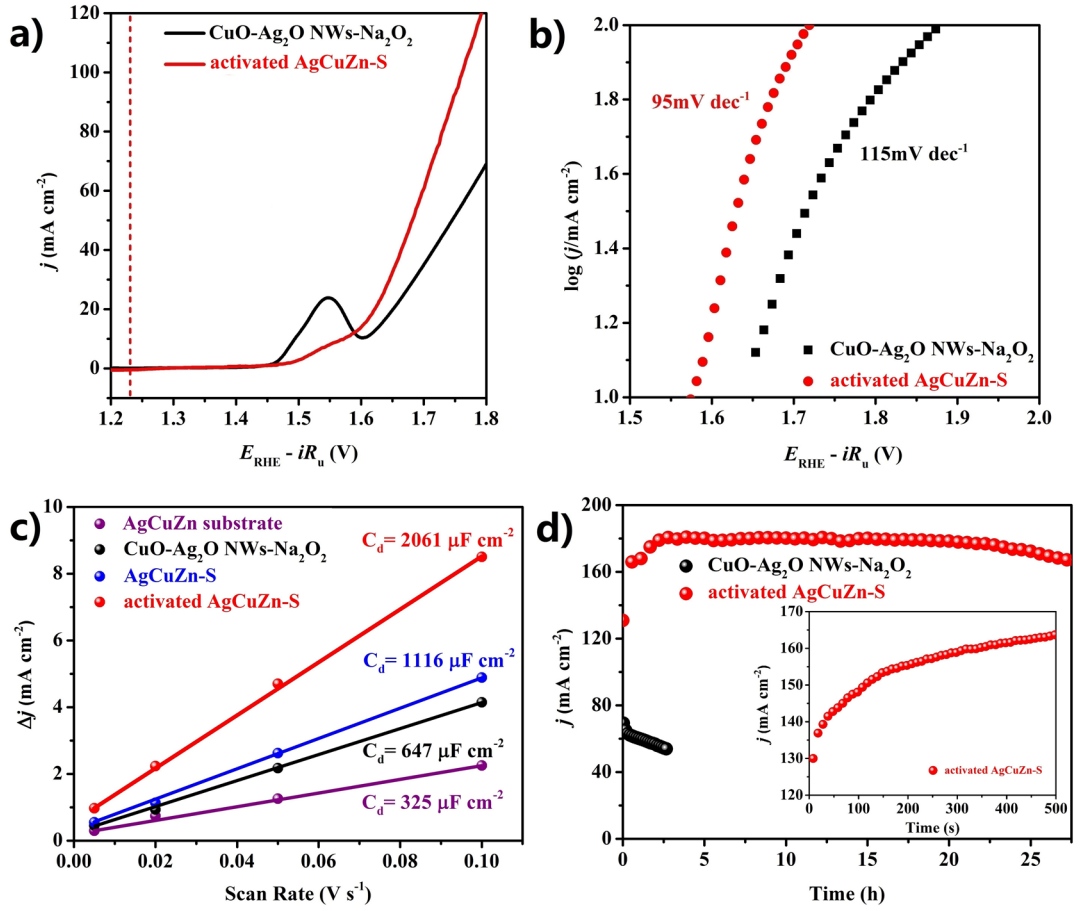

Figure 8. (a) LSV curves of CuO−Ag_2O NWs−Na_2O_2 and activated AgCuZn−S. (b) Tafel plots displaying the superior catalytic activity of activated AgCuZn−S to CuO−Ag_2O NWs−Na_2O_2. (c) The charging currents under different scanning rates of bare AgCuZn alloy substrate, CuO−Ag_2O NWs−Na_2O_2, AgCuZn−S, and activated AgCuZn−S. (d) Stability of catalysts. The inset is the change of the current density of activated AgCuZn−S (after activation for 800 s in Figure 7a) in the initial 500 s. The electrolysis tests are maintained at 1.8 V versus RHE in 1.0 M KOH electrolyte.

until 8000 s (2.2 h). After 8000 s, the current density becomes almost constant until 50 000 s (13.8 h). From 50 000 to 100 000 s, the current density goes through a decline and finally gets down to ∼160 mA cm^{-2} (around 130% of initial value after 10 000 s), which is highly superior to the CuO−Ag_2O NWs−Na_2O_2 (gets down to below 80% of initial value). The result indicates that the activated AgCuZn−S maintains an outstanding long-term durability for water oxidation in an alkaline medium over a prolonged period. Moreover, the comparison of EIS spectra of CuO−Ag_2O NWs−Na_2O_2 and activated AgCuZn−S is shown in Figure S11 of the SI.

4. CONCLUSION

AgCuZn sulfide particles are fabricated through a simple hydrothermal sulfuration process for water oxidation. The mixed alloy sulfide displays a current density of 40 mA cm^{-2} at a potential of 1.66 V versus RHE (η = 0.43 V) and a current density of 50 mA cm^{-2} at 1.68 V versus RHE (η = 0.45 V) as well as a Tafel slope of 95 mV dec^{-1} after a remarkable electrochemical activation. At the same time, the activated alloy sulfide exhibits excellent electrocatalytic stability and long-term stability, with the current density increasing by ∼30% as a whole after the electrolysis test for more than 27 h. Furthermore, the electrochemical activation process is systematically investigated through SEM, HRTEM, XRD, XPS, and EDS, which indicates a conspicuous transformation from alloy sulfide particles into CuO−Ag_2O NW arrays on the surface of the electrode. This transformation promotes the conductivity of mass transfer and electrochemical active area of the electrode catalyst, which further increases the catalytic activity of the catalyst. Therefore, this as-prepared electrode catalyst may become a promising anode in alkaline electrolysis of water in the future.

■ ASSOCIATED CONTENT

Supporting Information

HRTEM images of AgCuZn sulfide and CuO−Ag_2O NW arrays, XRD patterns of silver sulfide and copper sulfide, LSV curves of the electrochemical activation process, Faradaic efficiency of activated AgCuZn sulfide, CV curves of four electrode samples, LSV curves of various alloy sulfide electrodes, CV curves of AgCuZn−S before and after activation, CV curves and EIS spectra of CuO−Ag_2O NWs−Na_2O_2 and activated AgCuZn−S, overpotentials and Tafel slopes of OER electrodes, data of the AgCuZn sulfides with different metallic proportions, EDS spectrum, and elemental ratio of the alloy sulfide before activation. The Supporting Information is available free of charge on the ACS Publications website at DOI: 10.1021/acsami.5b03805.

DOI: 10.1021/acsami.5b03805
ACS Appl. Mater. Interfaces 2015, 7, 17112−17121

AUTHOR INFORMATION

Corresponding Author

*E-mail: yongjin-scu@163.com.

Notes

The authors declare no competing financial interest.

ACKNOWLEDGMENTS

We gratefully acknowledge the Scientific Exploration Project for Undergraduates of Sichuan Province (no. 201410610177) for financial support. We also express our thanks to Mr. Chuan Xin of Chengdu Branch, Chinese Academy of Sciences, for taking the XPS spectra.

REFERENCES

(1) Suntivich, J.; May, K. J.; Gasteiger, H. A.; Goodenough, J. B.; Shao-Horn, Y. A Perovskite Oxide Optimized for Oxygen Evolution Catalysis from Molecular Orbital Principles. *Science* **2011**, *334*, 1383−1385.

(2) Kanan, M. W.; Nocera, D. G. In Situ Formation of an Oxygen-Evolving Catalyst in Neutral Water Containing Phosphate and Co^{2+}. *Science* **2008**, *321*, 1072−1075.

(3) Cook, T. R.; Dogutan, D. K.; Reece, S. Y.; Surendranath, Y.; Teets, T. S.; Nocera, D. G. Solar Energy Supply and Storage for the Legacy and Nonlegacy Worlds. *Chem. Rev.* **2010**, *110*, 6474−6502.

(4) Walter, M. G.; Warren, E. L.; McKone, J. R.; Boettcher, S. W.; Mi, Q.; Santori, E. A.; Lewis, N. S. Solar Water Splitting Cells. *Chem. Rev.* **2010**, *110*, 6446−6473.

(5) Smith, R. D.; Prevot, M. S.; Fagan, R. D.; Trudel, S.; Berlinguette, C. P. Water Oxidation Catalysis: Electrocatalytic Response to Metal Stoichiometry in Amorphous Metal Oxide Films Containing Iron, Cobalt, and Nickel. *J. Am. Chem. Soc.* **2013**, *135*, 11580−11586.

(6) Dau, H.; Limberg, C.; Reier, T.; Risch, M.; Roggan, S.; Strasser, P. The Mechanism of Water Oxidation: from Electrolysis via Homogeneous to Biological Catalysis. *ChemCatChem* **2010**, *2*, 724−761.

(7) Xu, P.; Han, X.; Zhang, B.; Du, Y.; Wang, H. L. Multifunctional Polymer-Metal Nanocomposites via Direct Chemical Reduction by Conjugated Polymers. *Chem. Soc. Rev.* **2014**, *43*, 1349−1360.

(8) Cheng, F.; Chen, J. Metal-Air Batteries: from Oxygen Reduction Electrochemistry to Cathode Catalysts. *Chem. Soc. Rev.* **2012**, *41*, 2172−2192.

(9) Kudo, A.; Miseki, Y. Heterogeneous Photocatalyst Materials for Water Splitting. *Chem. Soc. Rev.* **2009**, *38*, 253−278.

(10) Lewis, N. S.; Nocera, D. G. Powering the Planet: Chemical Challenges in Solar Energy Utilization. *Proc. Natl. Acad. Sci. U. S. A.* **2006**, *103*, 15729−15735.

(11) Lu, Y. C.; Xu, Z.; Gasteiger, H. A.; Chen, S.; Hamad-Schifferli, K.; Shao-Horn, Y. Platinum-Gold Nanoparticles: A Highly Active Bifunctional Electrocatalyst for Rechargeable Lithium-Air Batteries. *J. Am. Chem. Soc.* **2010**, *132*, 12170−12171.

(12) Smith, R. D.; Prevot, M. S.; Fagan, R. D.; Zhang, Z.; Sedach, P. A.; Siu, M. K.; Trudel, S.; Berlinguette, C. P. Photochemical Route for Accessing Amorphous Metal Oxide Materials for Water Oxidation Catalysis. *Science* **2013**, *340*, 60−63.

(13) Liang, Y.; Li, Y.; Wang, H.; Dai, H. Strongly Coupled Inorganic/Nanocarbon Hybrid Materials for Advanced Electrocatalysis. *J. Am. Chem. Soc.* **2013**, *135*, 2013−2036.

(14) Gray, H. B. Powering the Planet with Solar Fuel. *Nat. Chem.* **2009**, *1*, 7.

(15) Bockris, J. O.; Otagawa, T. Mechanism of Oxygen Evolution on Perovskites. *J. Phys. Chem.* **1983**, *87*, 2960−2971.

(16) Hamdani, M.; Singh, R.; Chartier, P. Co_3O_4 and Co-Based Spinel Oxides Bifunctional Oxygen Electrodes. *Int. J. Electrochem. Sci.* **2010**, *5*, 556−577.

(17) Dinca, M.; Surendranath, Y.; Nocera, D. G. Nickel-Borate Oxygen-Evolving Catalyst that Functions under Benign Conditions. *Proc. Natl. Acad. Sci. U. S. A.* **2010**, *107*, 10337−10341.

(18) Surendranath, Y.; Dinca, M.; Nocera, D. G. Electrolyte-Dependent Electrosynthesis and Activity of Cobalt-Based Water Oxidation Catalysts. *J. Am. Chem. Soc.* **2009**, *131*, 2615−2620.

(19) Brunschwig, B. S.; Chou, M. H.; Creutz, C.; Ghosh, P.; Sutin, N. Mechanisms of Water Oxidation to Oxygen: Cobalt(IV) as an Intermediate in the Aquocobalt(II)-Catalyzed Reaction. *J. Am. Chem. Soc.* **1983**, *105*, 4832−4833.

(20) Li, P.; Jin, Z.; Xiao, D. A One-Step Synthesis of Co-P-B/rGO at Room Temperature with Synergistically Enhanced Electrocatalytic Activity in Neutral Solution. *J. Mater. Chem. A* **2014**, *2*, 18420−18427.

(21) Jin, Z.; Li, P.; Huang, X.; Zeng, G.; Jin, Y.; Zheng, B.; Xiao, D. Three-Dimensional Amorphous Tungsten-Doped Nickel Phosphide Microsphere as an Efficient Electrocatalyst for Hydrogen Evolution. *J. Mater. Chem. A* **2014**, *2*, 18593−18599.

(22) Jin, Z. Y.; Li, P. P.; Xiao, D. Enhanced Electrocatalytic Performance for Oxygen Reduction via Active Interfaces of Layer-By-Layered Titanium Nitride/Titanium Carbonitride Structures. *Sci. Rep.* **2014**, *4*, 6712−6718.

(23) Marshall, A. T.; Haverkamp, R. G. Electrocatalytic Activity of IrO_2−RuO_2 Supported on Sb-Doped SnO_2 Nanoparticles. *Electrochim. Acta* **2010**, *55*, 1978−1984.

(24) Horkans, J.; Shafer, M. W. Investigation of the Electrochemistry of a series of Metal Dioxides with Rutile-Type Structure: MoO_2, WO_2, ReO_2, RuO_2, OsO_2, and IrO_2. *J. Electrochem. Soc.* **1977**, *124*, 1202−1207.

(25) Galizzioli, D.; Tantardini, F.; Trasatti, S. Ruthenium Dioxide: A New Electrode Material. I. Behaviour in Acid Solutions of Inert Electrolytes. *J. Appl. Electrochem.* **1974**, *4*, 57−67.

(26) Bikkarolla, S. K.; Papakonstantinou, P. $CuCo_2O_4$ Nanoparticles on Nitrogenated Graphene as Highly Efficient Oxygen Evolution Catalyst. *J. Power Sources* **2015**, *281*, 243−251.

(27) Louie, M. W.; Bell, A. T. An Investigation of Thin-Film Ni-Fe Oxide Catalysts for the Electrochemical Evolution of Oxygen. *J. Am. Chem. Soc.* **2013**, *135*, 12329−12337.

(28) Liang, Y.; Li, Y.; Wang, H.; Zhou, J.; Wang, J.; Regier, T.; Dai, H. Co_3O_4 Nanocrystals on Graphene as a Synergistic Catalyst for Oxygen Reduction Reaction. *Nat. Mater.* **2011**, *10*, 780−786.

(29) Zhao, Z.; Wu, H.; He, H.; Xu, X.; Jin, Y. Self-Standing Non-Noble Metal (Ni-Fe) Oxide Nanotube Array Anode Catalysts with Synergistic Reactivity for High-Performance Water Oxidation. *J. Mater. Chem. A* **2015**, *3*, 7179−7186.

(30) Jin, Z.; Li, P.; Zheng, B.; Yuan, H.; Xiao, D. CuO−Ag_2O Nanoparticles Grown on a AgCuZn Alloy Substrate In Situ for Use as a Highly Sensitive Non-Enzymatic Glucose Sensor. *Anal. Methods* **2014**, *6*, 2215−2220.

(31) Audichon, T.; Mayousse, E.; Morisset, S.; Morais, C.; Comminges, C.; Napporn, T. W.; Kokoh, K. B. Electroactivity of RuO_2−IrO_2 Mixed Nanocatalysts Toward the Oxygen Evolution Reaction in a Water Electrolyzer Supplied by a Solar Profile. *Int. J. Hydrogen Energy* **2014**, *39*, 16785−16796.

(32) Huang, X.; Xie, M.; Chen, Y.; Zong, Q.; Liu, Z.; Jin, Y. Copper-Silver Oxide Nanowires Grown On an Alloy Electrode as an Efficient Electrocatalyst for Water Oxidation. *RSC Adv.* **2015**, *5*, 26150−26156.

(33) Jankovic, L.; Dimos, K.; Bujdak, J.; Koutselas, I.; Madejova, J.; Gournis, D.; Karakassides, M. A.; Komadel, P. Synthesis and Characterization of Low Dimensional ZnS- and PbS- Semiconductor Particles on a Montmorillonite Template. *Phys. Chem. Chem. Phys.* **2010**, *12*, 14236−14244.

(34) Patel, J. D.; Mighri, F.; Ajji, A. Generalized Chemical Route to Develop Fatty Acid Capped Highly Dispersed Semiconducting Metal Sulphide Nanocrystals. *Mater. Res. Bull.* **2012**, *47*, 2016−2021.

(35) Pandit, P.; Rakshit, B.; Sanyal, S. P. Electronic and Elastic Properties of Alkali-Metal Sulphides-Li_2S and Na_2S. *Indian J. Pure Appl. Phys.* **2009**, *47*, 804−807.

(36) Di Paola, A.; Addamo, M.; Palmisano, L. Mixed Oxide/Sulfide Systems for Photocatalysis. *Res. Chem. Intermed.* **2003**, *29*, 467−475.

(37) Deshpande, A.; Gupta, N. M. Critical Role of Particle Size and Interfacial Properties in the Visible Light Induced Splitting of Water

DOI: 10.1021/acsami.5b03805
ACS Appl. Mater. Interfaces 2015, 7, 17112−17121

Over the Nanocrystallites of Supported Cadmium Sulphide. *Int. J. Hydrogen Energy* **2010**, *35*, 3287−3296.
(38) Zhang, K.; Guo, L. Metal Sulphide Semiconductors for Photocatalytic Hydrogen Production. *Catal. Sci. Technol.* **2013**, *3*, 1672−1690.
(39) Ikeda, S.; Nakamura, T.; Harada, T.; Matsumura, M. Multicomponent Sulfides as Narrow Gap Hydrogen Evolution Photocatalysts. *Phys. Chem. Chem. Phys.* **2010**, *12*, 13943−13949.
(40) Jin, Z.; Li, P.; Liu, G.; Zheng, B.; Yuan, H.; Xiao, D. Enhancing Catalytic Formaldehyde Oxidation on CuO−Ag_2O Nanowires for Gas Sensing and Hydrogen Evolution. *J. Mater. Chem. A* **2013**, *1*, 14736−14743.
(41) Barnett, S. M.; Goldberg, K. I.; Mayer, J. M. A Soluble Copper−Bipyridine Water-Oxidation Electrocatalyst. *Nat. Chem.* **2012**, *4*, 498−502.
(42) Innocenti, M.; Zafferoni, C.; Lavacchi, A.; Becucci, L.; Di Benedetto, F.; Carretti, E.; Vizza, F.; Foresti, M. L. Electroactivation of Microparticles of Silver on Glassy Carbon for Oxygen Reduction and Oxidation Reactions. *J. Electrochem. Soc.* **2014**, *161*, D3018−D3024.
(43) Gorlin, Y.; Jaramillo, T. F. A Bifunctional Nonprecious Metal Catalyst for Oxygen Reduction and Water Oxidation. *J. Am. Chem. Soc.* **2010**, *132*, 13612−13614.
(44) Zhuang, Z.; Su, X.; Yuan, H.; Sun, Q.; Xiao, D.; Choi, M. M. An Improved Sensitivity Non-Enzymatic Glucose Sensor Based on a CuO Nanowire Modified Cu Electrode. *Analyst* **2008**, *133*, 126−132.
(45) Yin, M.; Wu, C. K.; Lou, Y.; Burda, C.; Koberstein, J. T.; Zhu, Y.; O'Brien, S. Copper Oxide Nanocrystals. *J. Am. Chem. Soc.* **2005**, *127*, 9506−9511.
(46) Xu, M.; Han, L.; Dong, S. Facile Fabrication of Highly Efficient g-C_3N_4/Ag_2O Heterostructured Photocatalysts with Enhanced Visible-Light Photocatalytic Activity. *ACS Appl. Mater. Interfaces* **2013**, *5*, 12533−12540.
(47) Lalitha, K.; Reddy, J. K.; Sharma, M. V. P.; Kumari, V. D.; Subrahmanyam, M. Continuous Hydrogen Production Activity over Finely Dispersed Ag_2O/TiO_2 Catalysts from Methanol: Water Mixtures Under Solar Irradiation: A Structure-Activity Correlation. *Int. J. Hydrogen Energy* **2010**, *35*, 3991−4001.
(48) Wang, Q.; An, N.; Bai, Y.; Hang, H.; Li, J.; Lu, X.; Liu, Y.; Wang, F.; Li, Z.; Lei, Z. High Photocatalytic Hydrogen Production from Methanol Aqueous Solution Using the Photocatalysts CuS/TiO_2. *Int. J. Hydrogen Energy* **2013**, *38*, 10739−10745.
(49) Gholami, M.; Qorbani, M.; Moradlou, O.; Naseri, N.; Moshfegh, A. Z. Optimal Ag_2S Nanoparticle Incorporated TiO_2 Nanotube Array for Visible Water Splitting. *RSC Adv.* **2014**, *4*, 7838−7844.
(50) Zhang, M. T.; Chen, Z. F.; Kang, P.; Meyer, T. J. Electrocatalytic Water Oxidation with a Copper(II) Polypeptide Complex. *J. Am. Chem. Soc.* **2013**, *135*, 2048−2051.
(51) Benck, J. D.; Chen, Z.; Kuritzky, L. Y.; Forman, A. J.; Jaramillo, T. F. Amorphous Molybdenum Sulfide Catalysts for Electrochemical Hydrogen Production: Insights into the Origin of Their Catalytic Activity. *ACS Catal.* **2012**, *2*, 1916−1923.

DOI: 10.1021/acsami.5b03805
ACS Appl. Mater. Interfaces 2015, 7, 17112−17121